Materials Today Chemistry 29 (2023) 101404

Contents lists available at ScienceDirect

Materials Today Chemistry

journal homepage: www.journals.elsevier.com/materials-today-chemistry/

Synergistic assembly of gold and copper-iron oxide nanocatalysts to promote the simultaneous depletion of glucose and glutathione

J. Bonet-Aleta [a, b, c], J.L. Hueso [a, b, c, *], L. Sanchez-Uriel [a, b, c], M. Encinas-Gimenez [a, b, c], S. Irusta [a, b, c], P. Martin-Duque [b, d, e, f], G. Martinez [a, b, c], J. Santamaria [a, b, c, **]

[a] Instituto de Nanociencia y Materiales de Aragon (INMA) CSIC-Universidad de Zaragoza, Campus Rio Ebro, Edificio I+D, C/ Poeta Mariano Esquillor, S/n, 50018, Zaragoza, Spain
[b] Networking Res. Center in Biomaterials, Bioengineering and Nanomedicine (CIBER-BBN), Instituto de Salud Carlos III, Madrid, 28029, Spain
[c] Department of Chemical and Environmental Engineering, Campus Rio Ebro, University of Zaragoza, Campus Rio Ebro, C/Mariano Esquillor, s/n, Zaragoza, 50018, Spain
[d] Instituto de Investigación Sanitaria (IIS) de Aragón, Avenida San Juan Bosco, 13, 50009, Zaragoza, Spain
[e] Fundación Araid. Av. de Ranillas 1-D, 50018 Zaragoza, Spain
[f] Departamento de Cirugía, Facultad de Medicina, Universidad de Zaragoza, 50009 Zaragoza, Spain

ARTICLE INFO

Article history:
Received 2 August 2022
Received in revised form
10 January 2023
Accepted 15 January 2023
Available online xxx

Keywords:
Glucose oxidation
GSH oxidation
Cancer therapy
Cascade reactions

ABSTRACT

Glucose and glutathione (GSH) are key biomolecules for the regulation and growth of tumor cells. The use of inorganic nanocatalysts in biomedicine to target and deplete such specific molecules represents a novel and promising strategy against cancer. In this work, we present a ternary assembled nanohybrid based on Au and $CuFe_2O_4$ with the capability to simultaneously deplete glucose and GSH and generate reactive oxidative species (ROS) in a cascade process. We describe an example of a synergistic heterogeneous nanoarchitecture able to maintain the glucose oxidase-like activity of Au while preventing its deactivation in the presence of GSH. Au sites remain active due to the rapid response of the Cu–Fe co-catalyst to deplete GSH levels. This example of hybrid heterostructure represents an appealing alternative with dual-activity within the tumor microenvironment (TME) for potential anticancer therapy.

1. Introduction

The development of inorganic nanocatalysts in biomedicine has irrupted as a promising alternative for multiple therapies such as antibacterial, anti-inflammatory, Alzheimer or brain disease and even tissue engineering or diagnostic imaging [1]. Cancer still represents the most challenging systemic disease faced by human mankind and the number of catalytic materials devoted to this endeavour has increased exponentially in the past few years [2]. In this context, the unique chemistry featuring the tumor microenvironment (TME) offer a powerful opportunity for engineered nanocatalysts to selectively induce cancer cell death by targeting key metabolites and biomolecules [3]. Moreover, the erratic and accelerated metabolism of tumor cells require an enormous and continuous energy supply, mainly in the form of glucose via aerobic glycolysis [4]. This is also known as Warburg effect and the principal consequence is a large glucose uptake by cancer cells. Thus, one of the most employed catalytic strategies consists in reducing glucose levels through its catalytic oxidation to cut off the ATP production-flux of the cancer cell [4,6]. Among the inorganic catalysts reported for glucose starvation therapy, freestanding and supported Au nanoparticles (Au NPs) represent the most active alternative to natural enzymes with a glucose oxidase mimicking response [7–10]. While this catalytic activity is well established, the potential influence of sulphur-containing biomolecules present in the TME such as glutathione (GSH) [11,12] is typically overlooked. Sulphur strongly binds to the Au surface hence blocking and "poisoning" the active sites for glucose oxidation [13,14]. As a result, the potential use of Au NPs for starvation therapy becomes less effective.

Another interesting feature of the glucose oxidation process catalyzed by Au NPs is related with the generation of hydrogen (H_2O_2) as reaction by-product [10]. Most of the literature reports

Abbreviations: GSH, Glutathione; ROS, Reactive Oxygen Species; TME, Tumor Microenvironment; CDT, Chemodynamic Therapy.

* Corresponding author.
** Corresponding author.
E-mail addresses: jlhueso@unizar.es (J.L. Hueso), jesus.santamaria@unizar.es (J. Santamaria).

https://doi.org/10.1016/j.mtchem.2023.101404

exploiting glucose depletion typically combine Au nanoparticles with transition metals to decompose the generated H_2O_2 into hydroxyl radicals (•OH) via Fenton-like catalysis in a cascade reaction process [7–9]. The generated •OH are highly-reactive species that can irreversibly modify key biomolecules such as lipids, proteins or nucleic acids leading to cell apoptosis [15]. Nevertheless, considering the previously mentioned issue regarding Au deactivation with GSH, this molecule represents a severe obstacle to achieve an effective starvation therapy. On the other hand, the catalytic targeting of GSH with the aid of transition metal catalysts is becoming a potential anticancer strategy itself [16]. GSH is a key antioxidant molecule strongly involved in the regulation and damage prevention from Reactive Oxygen Species (ROS) generated in cancer cells [17]. Thus, the potential development of co-catalysts that can transform GSH into its dimeric GSSG form (Fig. 1) may represent an advantageous "two birds-one stone" scenario to prevent Au deactivation while enhancing oxidative stress due to the depletion of GSH levels. If terminal thiol groups from GSH evolve into -S-S- groups, the blockage of Au sites might be minimized. The aim of this work has been the design and development of a nanocatalytic hybrid platform combining Au NPs and copper-iron oxide (CuFe) NPs with specific response towards glucose and GSH, respectively. We intended to prevent the deactivation of Au under GSH levels typically found in the TME and provide a synergistic response towards the simultaneous depletion of both key biomolecules.

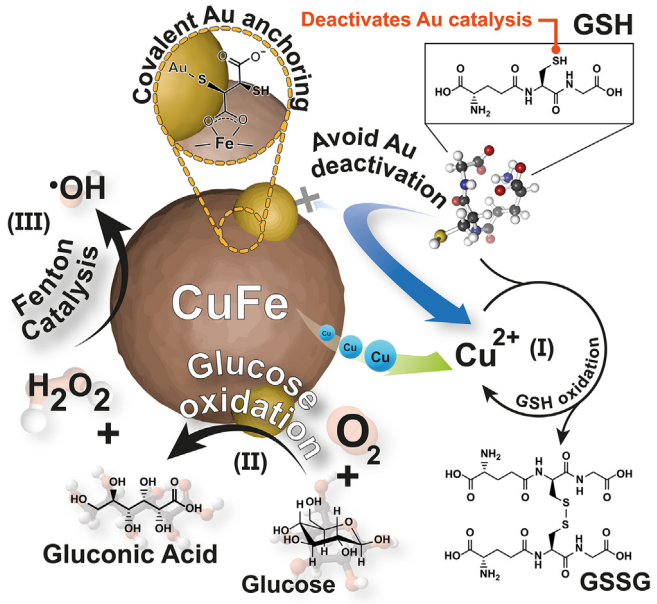

Fig. 1. Summary of the proposed catalytic reactions and mechanisms involved in the simultaneous depletion of glucose and GSH and the generation of hydroxyl radicals in the presence of the CuFe–Au nanohybrid linked via DMSA: SH group from GSH is responsible of deactivate Au nanoparticles and thus inhibiting their glucose oxidase-like activity. However, after deposition of Au on CuFe, the large affinity of GSH by Cu provokes their catalytic oxidation (step I) to avoid Au poisoning, which is then able to catalyze glucose oxidation (step II); Since H_2O_2 in one of the glucose oxidation by-products, CuFe nanoparticle can transform it into •OH in a reaction cascade (step III).

2. Experimental section

2.1. Chemicals

Iron (III) chloride hexahydrate ($FeCl_3 \cdot 6H_2O$, 97%), copper (II) chloride dihydrate ($CuCl_2 \cdot 2H_2O$, ≥99.0%), sodium acetate anhydrous (CH_3COONa, 99.0%), Bovine Serum Albumin (BSA), ethylene glycol (EG), Dimercaptosuccinic Acid (DMSA, 99.0%), Gold (III) chloride hydrate (50% Au basis), Tetrakis (hydroxymethyl) phosphonium chloride solution (THPC, 80 wt%, Germany), Tetraethyl orthosilicate (TEOS, ≥99.0%, GC), (3-aminopropyl)triethoxysilane (APTES, 99%), 3,3′,5,5′-tetramethylbenzidine (TMB, ≥95%), Glutathione (GSH), 5,5′-Dithiobis (2-nitrobenzoic acid) (DNTB), hydrogen peroxide (H_2O_2, 33% v/v), sodium bicarbonate ($NaHCO_3$, 99%), Tetraethyl orthosilicate (TEOS, ≥99.5% GC), were purchased from Sigma Aldrich. D-glucose was purchased from MP-biomedicals. Acetonitrile (ACN) was purchased from VWR (Avantor). Sodium phosphate monobasic (NaH_2PO_4, ≥99.0) and Potassium phosphate dibasic (K_2HPO_4, ≥99.0) were purchased from Fisher Chemical. Deuterium Oxide (D_2O, ≥99.9% in D) was purchased from Cambridge Isotope Laboratories. UPLC grade water was obtained from a Milli-Q Advantage A10 System with resistivity of 18.2 mΩ (Merk Millipore, Germany).

2.2. Characterization techniques

Transmission electron microscopy (TEM) was performed using a FEI TECNAI T20 microscope (Tecnai, Eindhoven, The Netherlands) operated at 200 keV. Aberration-corrected scanning transmission electron microscopy (Cs-corrected STEM) images were acquired using a high angle annular dark field detector (HAADF) in a FEI XFEG TITAN electron microscope (FEI, Eindhoven, The Netherlands) operated at 200–300 kV. Elemental analysis was carried out with an EDAX detector in scanning mode. Samples were prepared by drop casting 3–5 μL of the NPs suspension onto a holey carbon TEM grid. UV–vis spectra were obtained on a V67 UV–vis double beam spectrophotometer (JASCO, Madrid, Spain). Individual particle size was measured using ImageJ software. X-ray photoelectron spectroscopy (XPS) to analyze the surface of the nanohybrid was carried out with the aid of an AXIS Supra (Kratos Tech., Manchester, UK) using a monochromatic Al-Kα source (1486.6 eV) run at 8 kV and 10 mA. For the individual peak regions, a pass energy of 20 eV was used. Peaks analysis was performed with the CasaXPS software, using a weighted sum of Lorentzian and Gaussian components curves after Shirley background subtraction. The binding energies were referenced to the internal C1s (284.5 eV) standard. Cu, Fe and Au contents were measured on a 4100 MPAES instrument (Agilent, Madrid, Spain) after dissolving the sample in a mixture 5:1 of H_2O:aqua regia. Empyrean equipment in Bragg-Brentano configuration using CuKα radiation and equipped with a PIXcel1D detector. Raman spectroscopy was performed using alpha300 R, Raman Imaging Microscope, (WITec, Germany). Experimental conditions for CuFeAu, Au and Si were 785 nm laser source, 2 mW power, 3 s exposure time and 5 accumulations. For $CuFe_2O_4$, conditions were 532 nm laser wavelength, 5 mW, 10 s exposure time and 3 accumulations. ^1H NMR spectra were acquired using a Bruker AV-500 MHz NMR spectrometer.

2.3. Synthesis of CuFe-DMSA nanoparticles

250 mg of BSA were dissolved in 2.5 mL of miliQ water for 10 min and mixed with 12.5 mL of Ethylene glycol. Then, 270.0 mg of $FeCl_3 \cdot 6H_2O$, 85.0 mg of $CuCl_2$ and 375.0 mg of CH_3COONa were added into the reaction flask. The reaction was stirred for 2 h at room temperature. Then, the reaction was transferred to a Teflon autoclave where the temperature was set to 180 °C for 24 h. Finally, the product was centrifuged at 12 000 rpm for 20 min. DMSA ligand (20 mL, 25 mM) and 5 mL of 0.7 M NaOH solution were added to the obtained suspension using ultrasonication for 5 min. The final product was purified by two centrifugation cycles at 12,000 rpm for 20 min. The resulting solid was stored at 4 °C until further use.

2.4. Synthesis of ultrasmall Au nanoparticles

The preparation of ultrasmall Au nanoparticles was performed following previous group work protocols [10,18]. Briefly, to a total volume of 14 mL of distilled water, 165 μL of a 1 M NaOH solution, 333 μL of a 65 mM THPC solution and 1 mL of a $HAuCl_4 \cdot x\ H_2O$ (3 mg/mL) solution were sequentially added. Time between the addition of THPC and Au precursor was fixed to 2 min. The reaction mixture was stirred overnight at room temperature and directly used to fabricate CuFe–Au nanostructures.

2.5. Assembly of CuFe–Au nanohybrids

In a total volume of 2 mL, 750 μL of Au-THPC nanoparticles solution was mixed with 250 μL of CuFe-DMSA. The pH was adjusted to 7.4 using a 0.1 M HCl solution. Final solution stirred overnight at room temperature. CuFe–Au nanoparticles were purified by centrifugation (13 300 rpm, 10 min, twice) and were resuspended in 2 mL of miliQ H_2O.

2.6. Catalytic glucose oxidation

Elimination of glucose by CuFe–Au catalyst was analyzed according to the following method. 5.5 mM of glucose were mixed with 0.1 mg/mL of CuFe–Au in a total volume of 2.5 mL at 37 °C, using Phosphate Buffer Saline as medium (pH = 7.4). Glucose concentration at different reaction times was measured by UPLC-QDa detector. 20 μL of reaction were sampled and mixed with 955 μL of a mixture 1:1 Acetonitrile:H_2O and with 25 μL of a lactose 1000 ppm solution as internal standard.

2.7. Catalytic GSH depletion

Catalytic activity towards GSH oxidation of CuFe–Au nanoparticles was evaluated according to the following protocol: 5 mM of GSH were mixed with 0.1 mg/mL of CuFe–Au in a total volume of 2.5 mL at 37 °C. GSH concentration at different reaction times was measured by UPLC-PDA detector. 20 μL of reaction were mixed with 100 μL of Di-sulfanediylbis-(2-nitrobenzoic acid) (DTNB) and 880 μL of 0.01 M 2-amino-2-hydroxymethyl propane 1,3 diol (TRIS).

2.8. UPLC-PDA-MS equipment for glucose and GSH analysis

Glucose and GSH analysis were performed on Waters ACQUITY system H-Class that consisted of a binary pump, an autosampler, a column thermostat and a photodiode array (PDA) detector. This system is coupled to a single quadrupole mass spectrometer with an electrospray ionization (ESI) ACQUITY QDa mass detector. Glucose was monitored through its adduct $[M+Cl]^-$ at m/z = 215.15 (see Fig. S1). Data acquisition and processing were performed by using MASSLYNX software (Waters Corporation USA). On the one hand, in order to analyze GSH from derivatized samples (*vide infra*), chromatographic separation was performed using an ACQUITY UPLC BEH C18 column (130 Å, 1.7 μm 2.1 × 50 mm, from WATERS) at 40 °C under an isocratic flow of 0.3 mL/min containing 50% acetonitrile, 50% milli Q water. PDA detector was employed to monitor the absorbance from derivatized GSH at 412 nm during analysis time (see Fig. S2). On the other hand, glucose was monitored after chromatographic separation using an ACQUITY UPLC BEH Amide column (130 Å, 1.7 μm, 2.1 mm × 100 mm, WATERS). In this case, the mobile phase consisted of an initial mixture of acetonitrile/water (90:10), containing 0.1% 10 mM ammonium chloride as a mobile phase modifier, at a 0.5 mL/min initial flow rate. A gradient in the mobile phase was employed to separate the different metabolites present in the samples. Water composition increased for 3 min until a 65% acetonitrile was reached and then the system recovered initial conditions. ACQUITY QDa mass detector was employed to quantify sugar concentrations according to the most abundant ions generated as described below. Calibrations were performed using commercial standards of glucose and lactose.

2.9. GSH derivatization protocols for UPLC analysis

The derivatization of GSH using DTNB yields a quantifiable yellow-colored product, 5-thiobis-(2-nitrobenzoic acid) (TNB^{2-}) which absorbs at 412 nm (see Fig. S3). 20 μL of reaction were mixed with 100 μL of 5,5′-Disulfanediylbis (2-nitrobenzoic acid) (DTNB) and 880 μL of 0.01 M 2-Amino-2-hydroxymethyl-propane-1,3-diol (TRIS). Both samples and standards were filtered with 0.22 μm Nylon filters before injecting in UPLC system.

2.10. ^1H NMR analysis of catalytic GSH oxidation

A 50 mM K_2HPO_4, 50 mM NaH_2PO_4 and 20 mM GSH solution was prepared in D_2O. Then, the CuFe catalyst was added until reaching a [Cu] = 2.0 μg/mL. Samples were collected at reaction times of 5 and 7 h and then centrifuged for 10 min at 13 000 rpm). Supernatant was filtered using 0.22 μm Nylon filters and incubated with 400 mg of Chelex resin for 30 min prior to the NMR analysis.

2.11. TMB oxidation assays

A freshly prepared TMB (5 mg dissolved in 1 mL of DMSO) solution was used before each assay. 2.3 mL of CH_3COONa (0.05 M) solution at pH = 5.80 were mixed with 200 μL of CuFe–Au solution (final Au concentration = 0.01 mg/mL) and 15 μL of TMB solution to reach a final concentration of 0.10 mM. Absorbance at 652 nm was monitored for 500 s to check the generation of oxidized TMB.

2.12. Cell viability experiments

Cells were maintained by the UC Berkeley Tissue Culture Facility. A-549 and CCD-32Sk cells were seeded in 75% and 85% confluence, respectively using Dulbecco's modified Eagle medium (DMEM supplemented with Glutamax) in a 96-well cell plate. CuFeAu NPs stock solution was centrifuged and the solid was dissolved in DMEM at different concentrations, ranging from 0.1 to 0.0125 mg/mL of Cu. After 48 h, the wells were washed with PBS. Then, 100 μL of solution containing CCK-8 in DMEM (10% v/v) was added to the well. The cell plate was incubated at 37 °C in a 5% CO_2 for 2.5 h (for A-549 cells) and 3.5 h (for CCD-32Sk cells). Finally, the absorbance at 450 nm was measured using a plate reader.

2.13. Internalization capacity of A549 cells and confocal imaging

Briefly, 20,000 A-549 cells were seeded onto Ø 12 mm coverslips, which were deposited on a 24-well plate. Cells were allowed to attach to the coverslip at 37 °C and 5% CO_2 and, 48 h after the seeding, cells were treated with a suspension of CuFe–Au NPs in DMEM at 6.25 μg/ml of Cu for 48 h (for control cells, media renewal was carried out). After this time, cells were washed thrice with PBS, fixed with 4% paraformaldehyde for 30 min, and washed again thrice with DPBS. Preparation of the samples for confocal microscopy assay included an initial permeabilization of the samples in a solution of DPBS/1% BSA/0.1% saponine, followed by a 1 h incubation with phalloidin-Alexa 488 (dilution 1:200) for actin fibres staining. After the incubation, coverslips were gently

deposited onto a drop of mounting media (Fluoromount-G) which also contained DAPI for nuclei staining. Regarding the CuFe–Au NPs, aggregates could be detected due to the reflection of the incident light. In order to ensure the internalization of the NPs in the cells, a Z-Stack of the whole cell was performed. Images were analyzed, and the maximum orthogonal projection was obtained for each image. The NPs could be observed due to the contrast detected with the photomultiplier for transmitted light (T-PMT). This experiment was performed in a confocal microscope (ZEISS LSM 880 Confocal Microscope), using a 63/1.4 Oil DIC M27 objective.

3. Results and discussion

3.1. Synthesis, assembly and characterization of the CuFe–Au nanocatalyst

We have fabricated a CuFe oxide spinel with reported activity and selectivity towards GSH oxidation [19] and modified its surface with dimercaptosuccinic acid (DMSA) as linker to subsequently attach ultrasmall Au NPs through covalent bonding (Fig. 1). We analyzed in previous works how GSH interacted with Cu–Fe in a first step (Fig. 1-I), and promoted the release of Cu^{2+} ions from the spinel network. These cations subsequently oxidized GSH into GSSG through homogeneous catalysis (Fig. 1-I). At this point, we hypothesized that this strong affinity between Cu and GSH [20] might prevent the excessive inactivation of Au sites induced by thiol groups from GSH during the glucose oxidation process (Fig. 1-II). In addition, we also demonstrated that the H_2O_2 generated as by-product during the glucose oxidation could be further transformed into $^{\bullet}OH$ through a cascade reaction (Fig. 1-III). The synthesis of the ternary CuFe–Au nanocatalyst took place following a two-stage process (Fig. 2). The first part consisted on the hydrothermal preparation of the Cu–Fe spinel oxide NPS using BSA as stabilizing agent [19] (Fig. 2a–i). Then, CuFe-BSA NPs were functionalized with DMSA [21] in a basic solution (Experimental section and Fig. S4). The ligand exchange and coating of CuFe-BSA NPs with DMSA took place through bonding between the carboxylic end

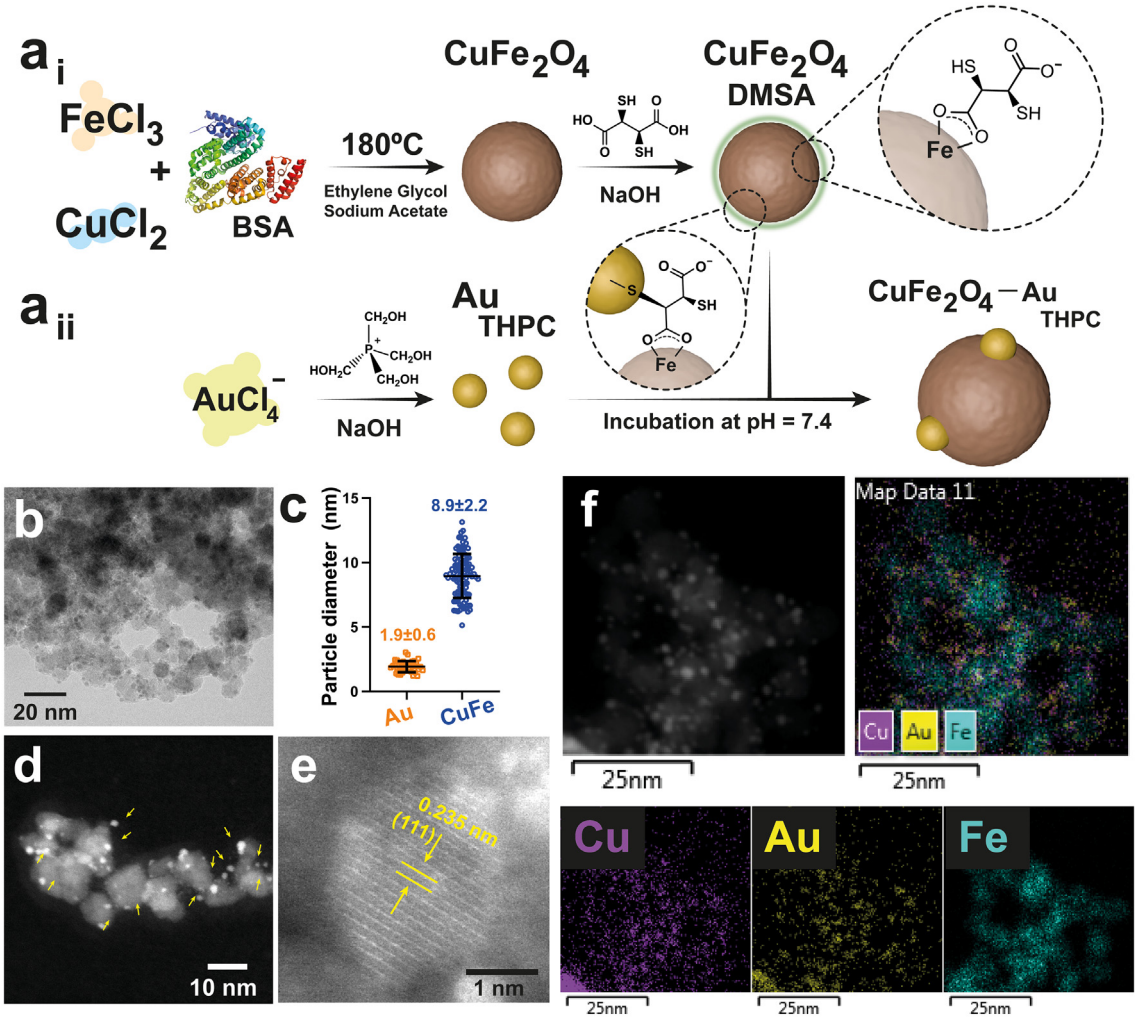

Fig. 2. Synthesis and electronic microscopy analysis of the CuFe–Au catalyst: (a) Scheme of the two-stage synthesis of the CuFe–Au nanohybrids: (a_i) Synthesis of the DMSA coated CuFe NPs using a hydrothermal assisted protocol in the presence of BSA, acting as template to induce particle growth at 180 °C and subsequent ligand exchange with DMSA in basic; (a_{ii}) Generation of Au NPs using THPC as simultaneous reducing and stabilizing agent in the presence of NaOH and final assembly of CuFe and Au NPs via Au–S covalent bonding. (b) TEM image of the CuFe–Au NPs; (c) Particle size distribution histograms corresponding to the individual diameters of AuNPs and CuFe NPs after attachment (n = 50); (d–e) HAADF-STEM of CuFe–Au nanocatalyst where ultrasmall Au NPs are pin-pointed with yellow arrows and (e) HR-STEM image of a single Au nanoparticle deposited on CuFe, where an interplanar distance of 0.235 nm can be attributed to the (111) plane of cubic structure of metallic Au; (f) STEM-EDS mapping analysis of CuFe–Au nanoparticles: Top row: HAADF-STEM image and EDS mapping distribution of Cu, Au and Fe (merged); Bottom row: specific mapping distribution for Cu, Au and Fe respectively.

groups and the Fe^{III} sites [21] of the spinel network (Fig. 2a–i). The second stage consisted in the synthesis of ultrasmall AuNPs using tetrakis-(hydroxymethyl)-phosphonium chloride (THPC) as reduction/stabilizing agent [10,18] (Fig. 2a–ii). Finally, both CuFe and Au NPs were assembled via covalent linking between the S–H terminal groups from DMSA and the Au NPs (Fig. 2 and SI for further details). Transmission electron microscopy (TEM) and High Angle Annular Dark Field Scanning Transmission Electron Microscopy (HAADF-STEM) analysis of the CuFe–Au nanohybrids confirmed the successful assembly (Fig. 2b and d-f) with an average diameter of 8.9 ± 2.2 nm and 1.9 ± 0.6 nm, respectively (Fig. 2c). HR-STEM analysis of individual Au NPs confirmed the (111) crystalline plane of cubic Au (Fig. 2e). The presence of Au was also confirmed by STEM-Electron Dispersive X-ray Spectroscopy (EDS) (Fig. 2f). STEM-EDS analysis of the nanohybrid (Fig. S5) also revealed a Cu:Fe:Au ratio of 1.0:1.6:0.3, respectively. In the same analysis performed by MP-AES, we obtained a Cu:Fe:Au ratio of 1.0:1.5:0.1, respectively. The XRD analysis also confirmed that the crystalline structure of the $CuFe_2O_4$ spinel was preserved after Au deposition. No clear signal from the Au NPs could be discerned given their reduced size (Fig. S6). X-ray photoelectron spectroscopy (XPS) analysis of the CuFe-DMSA NPs before and after the assembly of Au NPs corroborated the increase of Au atomic percent on the surface of the hybrid (see Tables S1–S2). Furthermore, the binding energies (BEs) centered at 84.4 and 87.9 eV confirmed the metallic nature of the Au species associated to the $Au4f_{7/2}$ and $Au4f_{5/2}$ regions, respectively [22] (Fig. 3a).

Two photoemission contributions at 85.2 and 88.6 eV were attributed to $Au^{\delta+}$ species probably in closer contact with the CuFe spinel [22] (Fig. 3a). XPS analysis of the Fe2p region revealed the coexistence of both divalent and trivalent oxidation states (Fig. 3b) with main contributions at 710.9 and 712.9 eV for $Fe(II)2p_{3/2}$ and $Fe(III)2p_{3/2}$, respectively [23]. Cu XPS spectra (Fig. 3c) showed a clear contribution of $Cu(II)2p_{3/2}$ and $Cu(I)2p_{3/2}$ at BEs of 934.9 and 933.5 eV [24]. Moreover, the assembly of Au nanoparticles did not alter the oxidation state of Fe and Cu (see Tables S3–S4). The S2p region (Fig. 3d and Tables S3–S4) disclosed three main doublet at 161.0 and 161.6 eV, attributed to S binding to Fe and Cu [25], 162.3 and 163.1 eV attributable to Au–S binding [26,27] and unbounded thiol groups at 163.8 ($S2p_{3/2}$) and 164.9 eV ($S2p_{1/2}$), respectively [28]. Finally, a contribution from oxidized species could be identified at higher BEs [28]. FTIR analysis mostly revealed different contributions from DMSA and THPC present in the nanohybrids (see Fig. 3e). Two main contributions from DMSA (asymmetric/symmetric contributions of C=O bond at 1560 and 1390 cm^1) [29,30] and THPC (O–H stretching/bending/deformation at 3250, 1630 and 1360 cm^1, respectively) [31] confirmed the presence of the organic linker and the stabilizing ligand of AuNPs. Raman spectroscopy of the $CuFe_2O_4$ NPs revealed the presence of contributions at low Raman shifts in the region between 200 and 400 cm^1 that could be attributed to Fe and Cu oxides [32] (Fig. S7). The hybrid CuFe–Au also revealed additional contributions in the 594-680 cm^1 region corresponding to Cu and Fe oxides with higher valence states. Additional Raman features appearing at 132 cm^1 can be attributed to a small presence of gold oxide (Au–O stretching/bending), chloride (Au–Cl stretching) and/or sulfide (Au–S stretching) [33].

3.2. Simultaneous conversion of GSH and glucose: synergistic influence of the CuFe NPs and comparison with inert SiO_2 NPs

Fig. 4a shows the glucose conversion levels achieved by the Au NPs either in the presence or in absence of CuFe NPs and/or GSH with analogous reaction kinetics (Fig. S8). The glucose-oxidase mimicking activity of the Au NPs in the absence of GSH rendered glucose conversions close to 25% when deposited on inert SiO_2 NPs (see Fig. 4a and Figs. S9–S10). This conversion rose up to ca. 50% glucose conversion after 90 min of reaction at pH 7.4 in saline buffer (Phosphate Buffer Saline, PBS) at physiological temperature (i.e. 37 °C) with the CuFe–Au nanohybrid. These values are in agreement with those reported in the literature [7–10]. Interestingly, the enhanced catalytic conversion of the CuFe–Au NPs can be probably

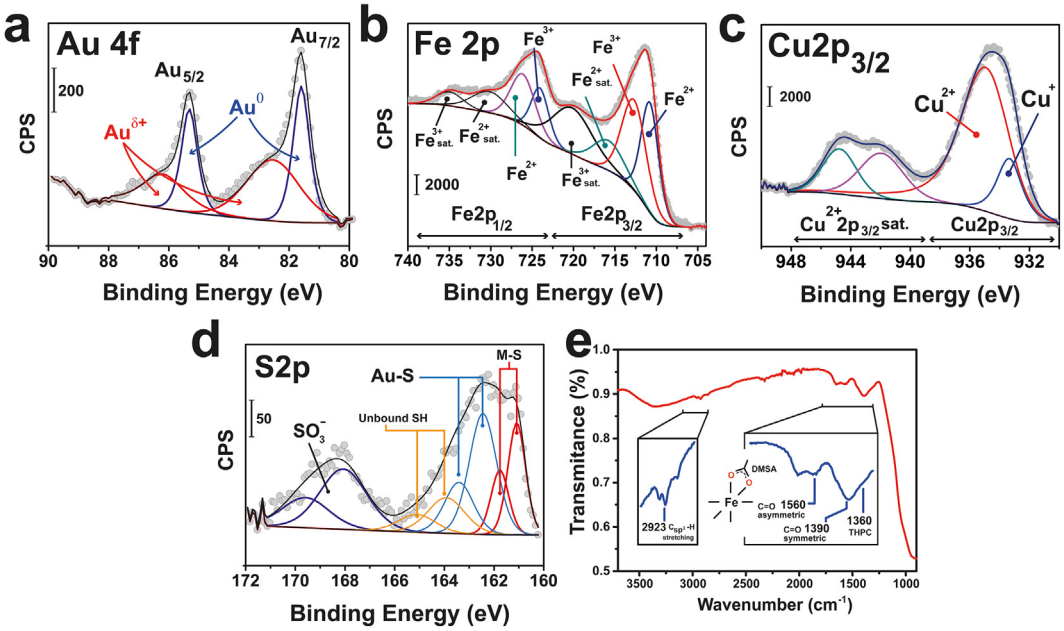

Fig. 3. Spectroscopic characterization of the CuFe–Au catalyst: (a) X-ray photoemission spectrum corresponding to the Au 4f region of CuFe–Au catalyst; (b) X-ray photoemission spectrum of the Fe2p region of the CuFe–Au catalyst accounting for the presence of divalent and trivalent Fe species; (c) X-ray photoemission spectrum of the $Cu2p_{3/2}$ region accounting for the presence of Cu(II) and Cu(I) species in the CuFe–Au catalyst; (d) X-ray photoemission spectrum of the S2p region where the peaks detected at higher binding energies (i.e. 162.5 and 163.6 eV) are attributed to Au–S bond formation [26,27]; (e) Fourier Transformed Infrared spectroscopy (FT-IR) analysis of the CuFe–Au nanohybrid.

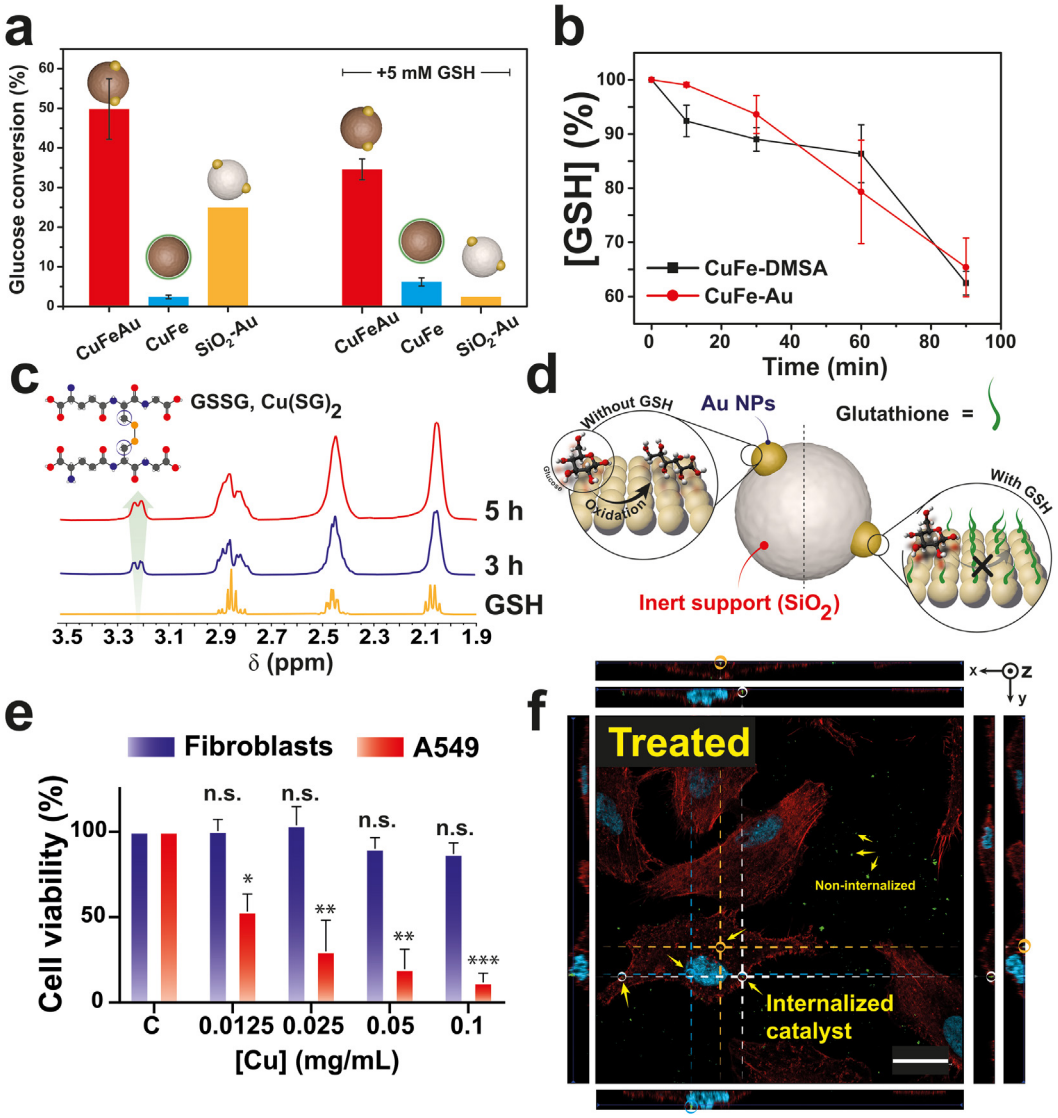

Fig. 4. Catalytic activity displayed by the DMSA-coated CuFe, CuFe–Au and SiO_2–Au nanocatalysts: (a) Glucose conversion in the presence and in the absence of GSH (5 mM) after 90 min; Reaction conditions: pH = 7.4, buffered PBS; $[Glucose]_0$ = 5.5 mM; $[GSH]_0$ = 5 mM; [Au] = 0.02 mg/mL; (b) GSH conversion levels before and after the assembly of Au NPs; (c) ^{1}H NMR analysis of GSH catalytic oxidation reaction at different reaction times. Signal at 3.20 ppm identifies as oxidized GSH (i.e. GSSG) or $Cu(SG)_2$ complex [20]; (d) Schematic illustration of the influence of GSH towards the deactivation of Au sites due to the competing poisoning induced by the GSH molecules that prevent the catalytic conversion of glucose; (e) Cell viability at different catalyst concentrations (expressed in [Cu]) after 48 h of incubation in A-549 (lung cancer cells, blue bar) and CCD-32Sk (human fibroblasts, red bar); (f) Confocal microscopy images obtained from treated A-549 cells with 6.25 mg Cu·mL^1 cells after 48 h. Actin fibres are shown in red after staining with phalloidin-Alexa 488, nuclei are displayed in light blue and stained with DAPI. CuFe–Au aggregates appear in green color and correspond to the reflected light. Top and right bar shows the profile of X and Y planes, respectively. Selected nanoparticles appear as non-internalized or exhibit co-location with red-actin fibers in the X, Y and Z plane. Scale bar = 20 μm.

attributed to the capacity of Cu and Fe to trigger a cascade reaction to transform H_2O_2, generated as secondary by-product of the glucose oxidation, into •OH. This latter process (see Fig. 1-III) would be favored via Fenton-like reaction [34] and would be contributing to the additional oxidation of glucose observed in Fig. 4a. In order to demonstrate this cascade reaction, we performed a series of experiments using the colorimetric probe 3,3′,5,5′-tetramethylbenzidine (TMB) whose reaction with oxidizing species (i.e. •OH) yields a colored probe that can be monitored by UV–vis spectroscopy (Fig. S11). A control experiment in the presence of 2 mM of H_2O_2 yielded an increase of the absorbance at 652 nm, due to the formation of the oxidized TMB species [10,12]. In the absence of H_2O_2, the enhancement of the signal could be only attributed to the oxidase-like capacity of the Au NPs, which can also transform TMB by themselves in the presence of dissolved O_2 [35]. However, in the presence of 5.5 mM of glucose, the absorbance at 652 nm was higher due to the progressive generation of H_2O_2 after catalyzing the glucose oxidation (Fig. S11).

Previous studies have demonstrated that GSH and other biomolecules containing –SH moieties [11] can induce the progressive deactivation of noble metals and the loss of their oxidase mimicking response [12–14]. In our case, the addition of GSH reduced the overall glucose conversion levels, regardless of the catalysts tested (Fig. 4a). Nevertheless, while the activity of the Au–SiO_2 NPs decreased in the presence of GSH (only 3% conversion was achieved after 90 min, a 9-fold decrease, see Fig. 4a), the CuFe–Au NPs were still able to achieve 35% glucose conversion (i.e. 70% of its original conversion) despite the strong deactivation

scenario induced by GSH. Moreover, these NPs were able to maintain the GSH depletion activity in comparison with the DMSA coated CuFe analogous NPs [19] (Fig. 4b). Furthermore, ^{1}H NMR analysis of the catalytic GSH oxidation showed an increasing contribution at 3.2 ppm due to the generation of $Cu(SG)_2$ and GSSG species, both present in the homogeneous GSH oxidation [20] (Fig. 4c). In summary, using CuFe NPs as co-catalyst of Au NPs delays their deactivation by GSH following the process illustrated in Fig. 4d. We hypothesize that both Au and CuFe NPs possess available active sites with strong affinity towards GSH. The preference of GSH to bind and with Cu sites [20] favors a delayed deactivation and poisoning of Au active sites that can continue the glucose conversion reaction in the presence of GSH and generate H_2O_2 for subsequent Fenton chemistry able to induce ROS generation. Likewise, the strong affinity of −SH group by Cu sites in the $CuFe_2O_4$ structure promotes its leaching following the reported mechanism in our previous work [20]. Once in solution, Cu^{2+} starts to catalyze oxidation of GSH to yield GSSG. We suggest that the decrease of free −SH groups from GSH after its oxidation can prevent the complete deactivation of the Au NPs towards the glucose oxidation.

Finally, the interaction of CuFeAu catalyst in a biological media was evaluated studying their cytotoxicity in A549 (lung cancer) and CCD-32Sk (human fibroblasts). A549 was the selected cancer cell line due to their known dependence on glycolysis [36] and GSH [37] metabolism. The viability of A549 cells decayed in the presence of CuFeAu catalyst while fibroblast remained healthy at all the evaluated concentrations of catalysts (Fig. 4e). We assume that the simultaneous depletion of both glucose and GSH have a direct impact on their survival and the high specificity towards the cancer cells corroborates the efficiency of the combined strategy targeting two key biomolecules for these cancer cells, simultaneously. Moreover, representative fluorescence confocal microscopy (Fig. 4f, Fig. S12) images of A549 incubated with CuFeAu NPs after 48 h demonstrated the presence of the catalyst within the cells to trigger the described catalytic reactions and also the presence of some non-internalized aggregates. All these data suggest CuFeAu as a promising and selective catalyst for Chemodynamic-starvation therapy.

4. Conclusions

We have demonstrated the versatility of a CuFe−Au nanoplatform able to simultaneously prevent the deactivation of Au sites during the catalytic oxidation of glucose and the oxidation of GSH. GSH is rapidly consumed due to the synergistic action of the Cu−Fe mixed oxide NPs assembled to the Au NPs. To the best of our knowledge, this is the first example in literature where this glucose conversion is successfully carried out in the presence of GSH [19,20]. The synergistic action of these heterostructures may pave the way to develop more efficient and selective nanocatalysts while preventing side effects or undesired deactivation events.

Credit author statement

J.B., J.L.H., L.S., M. E., P.M.D., G.M. and J.S.: Methodology; J.B. and J.L.H: Writing- Original draft preparation.; J.B., L.S., M.E. and J.L.H.: Investigation; J.B, J.L.H. and J.S.: Conceptualization; J.B. and J.L.H.: Analysis; J.S.: Funding. All authors reviewed the results and approved the final version of the manuscript.

Declaration of competing interest

The authors declare that they have no known competing financial interests or personal relationships that could have appeared to influence the work reported in this paper.

Data availability

Data will be made available on request.

Acknowledgements

Financial support from the European Research Council (ERC-Advanced Grant CADENCE number 742684) is acknowledged. The TEM measurements were conducted at the Laboratorio de Microscopies Avanzadas, ICTS ELECMI, Spain. The synthesis of materials has been performed by the Platform of Production of Biomaterials and Nanoparticles of the NANBIOSIS ICTS, more specifically by the Nanoparticle Synthesis Unit of the CIBER in BioEngineering, Biomaterials & Nanomedicine (CIBER-BBN). J.B-A. acknowledges the Spanish Government for an FPU predoctoral contract. M. E. acknowledges the Diputacion General de Aragon (DGA) for a predoctoral contract. The authors thank Dr. Javier Calzada for his help with UPLC measurements. The authors thank Prof. Christopher J. Chang from University of California, Berkeley for providing access to his laboratory facilities to perform NMR and cell viability experiments.

Appendix A. Supplementary data

Supplementary data to this article can be found online at https://doi.org/10.1016/j.mtchem.2023.101404.

References

[1] B. Yang, Y. Chen, J. Shi, Nanocatalytic Medicine, Adv. Mater. 31 (2019), 1901778.
[2] J. Chen, Y. Zhu, C. Wu, J. Shi, Nanoplatform-based cascade engineering for cancer therapy, Chem. Soc. Rev. 49 (2020) 9057−9094.
[3] H. Lin, Y. Chen, J. Shi, Nanoparticle-triggered in situ catalytic chemical reactions for tumour-specific therapy, Chem. Soc. Rev. 47 (2018) 1938−1958.
[4] R.J. DeBerardinis, N.S. Chandel, We need to talk about the Warburg effect, Nature Metabol. 2 (2020) 127−129.
[6] M.G. Vander Heiden, L.C. Cantley, C.B. Thompson, Understanding the Warburg effect: The metabolic requirements of cell proliferation, Science 324 (2009) 1029−1033.
[7] X. Wang, T. Xiong, M. Cui, X. Guan, J. Yuan, Z. Wang, R. Li, H. Zhang, S. Duan, F. Wei, Targeted self-activating Au-Fe3O4 composite nanocatalyst for enhanced precise hepatocellular carcinoma therapy via dual nanozyme-catalyzed cascade reactions, Appl. Mater. Today 21 (2020), 100827.
[8] S. Gao, H. Lin, H. Zhang, H. Yao, Y. Chen, J. Shi, Nanocatalytic tumor therapy by biomimetic dual inorganic nanozyme-catalyzed cascade reaction, Adv. Sci. 6 (2019), 1801733.
[9] X. Liu, Y. Pan, J. Yang, Y. Gao, T. Huang, X. Luan, Y. Wang, Y. Song, Gold nanoparticles doped metal-organic frameworks as near-infrared light-enhanced cascade nanozyme against hypoxic tumors, Nano Res. 13 (2020) 653−660.
[10] M.C. Ortega-Liebana, J. Bonet-Aleta, J.L. Hueso, J. Santamaria, Gold-based nanoparticles on amino-functionalized mesoporous silica supports as nanozymes for glucose oxidation, Catalysts 10 (2020).
[11] M.P. Gamcsik, M.S. Kasibhatla, S.D. Teeter, O.M. Colvin, Glutathione levels in human tumors, Biomarkers 17 (2012) 671−691.
[12] J. Bonet-Aleta, J.I. Garcia-Peiro, S. Irusta, J.L. Hueso, Gold-Platinum nanoparticles with core-shell configuration as efficient oxidase-like nanosensors for glutathione detection, Nanomaterials 12 (2022).
[13] Y. Zhao, Y. Huang, H. Zhu, Q. Zhu, Y. Xia, Three-in-One: sensing, self-assembly, and cascade catalysis of cyclodextrin modified gold nanoparticles, J. Am. Chem. Soc. 138 (2016) 16645−16654.
[14] Y. Lin, Z. Li, Z. Chen, J. Ren, X. Qu, Mesoporous silica-encapsulated gold nanoparticles as artificial enzymes for self-activated cascade catalysis, Biomaterials 34 (2013) 2600−2610.
[15] X. Wang, X. Zhong, Z. Liu, L. Cheng, Recent progress of chemodynamic therapy-induced combination cancer therapy, Nano Today 35 (2020), 100946.
[16] Y. Ding, Y. Dai, M. Wu, L. Li, Glutathione-mediated nanomedicines for cancer diagnosis and therapy, Chem. Eng. J. 426 (2021), 128880.
[17] J. Garcia-Bermudez, R.T. Williams, R. Guarecuco, K. Birsoy, Targeting extracellular nutrient dependencies of cancer cells, Mol. Metabol. 33 (2020) 67−82.
[18] J.L. Hueso, V. Sebastián, Á. Mayoral, L. Usón, M. Arruebo, J. Santamaría, Beyond gold: rediscovering tetrakis-(hydroxymethyl)-phosphonium chloride (THPC) as an effective agent for the synthesis of ultra-small noble metal nanoparticles and Pt-containing nanoalloys, RSC Adv. 3 (2013) 10427−10433.

[19] J. Bonet-Aleta, M. Sancho-Albero, J. Calzada-Funes, S. Irusta, P. Martin-Duque, J.L. Hueso, J. Santamaria, Glutathione-Triggered catalytic response of Copper-Iron mixed oxide Nanoparticles. Leveraging tumor microenvironment conditions for chemodynamic therapy, J. Colloid Interface Sci. 617 (2022) 704–717.
[20] J. Bonet-Aleta, M. Encinas-Gimenez, E. Urriolabeitia, P. Martin-Duque, J.L. Hueso, J. Santamaria, Unveiling the interplay between homogeneous and heterogeneous catalytic mechanisms in copper–iron nanoparticles working under chemically relevant tumour conditions, Chem. Sci. (2022).
[21] N. Miguel-Sancho, O. Bomatí-Miguel, G. Colom, J.P. Salvador, M.P. Marco, J. Santamaría, Development of stable, water-dispersible, and biofunctionalizable superparamagnetic iron oxide nanoparticles, Chem. Mater. 23 (2011) 2795–2802.
[22] I. Moreno, N. Navascues, S. Irusta, J. Santamaria, Electrospun Au/CeO2 nanofibers: a highly accessible low-pressure drop catalyst for preferential CO oxidation, J. Catal. 329 (2015) 479–489.
[23] K. Yuan, D. Lützenkirchen-Hecht, L. Li, L. Shuai, Y. Li, R. Cao, M. Qiu, X. Zhuang, M.K.H. Leung, Y. Chen, U. Scherf, Boosting oxygen reduction of single iron active sites via geometric and electronic engineering: nitrogen and phosphorus dual coordination, J. Am. Chem. Soc. 142 (2020) 2404–2412.
[24] M.C. Biesinger, Advanced analysis of copper X-ray photoelectron spectra, Surf. Interface Anal. 49 (2017) 1325–1334.
[25] R.S.C. Smart, W.M. Skinner, A.R. Gerson, XPS of sulphide mineral surfaces: metal-deficient, polysulphides, defects and elemental sulphur, Surf. Interface Anal. 28 (1999) 101–105.
[26] P. Gobbo, S. Novoa, M.C. Biesinger, M.S. Workentin, Interfacial strain-promoted alkyne–azide cycloaddition (I-SPAAC) for the synthesis of nanomaterial hybrids, Chem. Commun. 49 (2013) 3982–3984.
[27] P. Gobbo, Z. Mossman, A. Nazemi, A. Niaux, M.C. Biesinger, E.R. Gillies, M.S. Workentin, Versatile strained alkyne modified water-soluble AuNPs for interfacial strain promoted azide–alkyne cycloaddition (I-SPAAC), J. Mater. Chem. B 2 (2014) 1764–1769.
[28] L. Carlini, C. Fasolato, P. Postorino, I. Fratoddi, I. Venditti, G. Testa, C. Battocchio, Comparison between silver and gold nanoparticles stabilized with negatively charged hydrophilic thiols: SR-XPS and SERS as probes for structural differences and similarities, Colloids Surf. A Physicochem. Eng. Asp. 532 (2017) 183–188.
[29] L.N. Song, N. Gu, Y. Zhang, A moderate method for preparation DMSA coated Fe_3O_4 nanoparticles, IOP Conf. Ser. Mater. Sci. Eng. 164 (2017), 012026.
[30] S. Aryal, K.C.R. B, N. Dharmaraj, N. Bhattarai, C.H. Kim, H.Y. Kim, Spectroscopic identification of S-Au interaction in cysteine capped gold nanoparticles, Spectrochim. Acta Mol. Biomol. Spectrosc. 63 (2006) 160–163.
[31] W.W. Bryan, A.C. Jamison, P. Chinwangso, S. Rittikulsittichai, T.-C. Lee, T.R. Lee, Preparation of THPC-generated silver, platinum, and palladium nanoparticles and their use in the synthesis of Ag, Pt, Pd, and Pt/Ag nanoshells, RSC Adv. 6 (2016) 68150–68159.
[32] S. Rackauskas, A.G. Nasibulin, H. Jiang, Y. Tian, V.I. Kleshch, J. Sainio, E.D. Obraztsova, S.N. Bokova, A.N. Obraztsov, E.I. Kauppinen, A novel method for metal oxide nanowire synthesis, Nanotechnology 20 (2009), 165603.
[33] T.M. Devine, F. Adar, Raman Spectroscopy of Solids, Character. Mater. (2012) 1–38.
[34] Z. Tang, P. Zhao, H. Wang, Y. Liu, W. Bu, Biomedicine meets Fenton chemistry, Chem. Rev. 121 (2021) 1981–2019.
[35] X. Shen, W. Liu, X. Gao, Z. Lu, X. Wu, X. Gao, Mechanisms of oxidase and superoxide dismutation-like activities of gold, silver, platinum, and palladium, and their alloys: a general way to the activation of molecular oxygen, J. Am. Chem. Soc. 137 (2015) 15882–15891.
[36] M. Wu, A. Neilson, A.L. Swift, R. Moran, J. Tamagnine, D. Parslow, S. Armistead, K. Lemire, J. Orrell, J. Teich, S. Chomicz, D.A. Ferrick, Multiparameter metabolic analysis reveals a close link between attenuated mitochondrial bioenergetic function and enhanced glycolysis dependency in human tumor cells, American journal of physiology, Cell physiology 292 (2007) C125–C136.
[37] H.-x. Zhang, Y. Chen, R. Xu, Q.-y. He, Nrf2 mediates the resistance of human A549 and HepG2 cancer cells to boningmycin, a new antitumor antibiotic, in vitro through regulation of glutathione levels, Acta Pharmacol. Sin. 39 (2018) 1661–1669.